

Impact of Excitation and Weighting Errors on Performance of Compact OTA Testing Systems

Alejandro Antón Ruiz* and Andrés Alayón Glazunov*

*Department of Electrical Engineering, University of Twente, Enschede, The Netherlands

Abstract—This paper investigates the impact of complex excitation errors of the chamber array antenna on the accuracy of the test zone of a random line-of-sight over-the-air testing setup. First, several combinations of compact chamber arrays of lengths L and short distances D between the test zone and the chamber array, which emulate a plane wave impinging at the test zone are obtained. The chamber array is linear and uniform with 100 antenna elements, and a linear taper was applied to some of the elements to emulate a plane wave impinging at the test zone with more compact setups. A subset of L and D was chosen, providing compact over-the-air test setups that fulfilled the defined figures of merit, which assess the similarity of the obtained field distribution to that of a plane wave. The tolerance of the chosen setups to complex excitation errors of the chamber array was then investigated, concluding that these errors must be considered when defining appropriate L and D combinations. Moreover, the performance of the matched filter and zero-forcing algorithms is evaluated for errors of the device under test array weighting coefficients. A random line-of-sight over-the-air testing setup with two arrays was simulated, where one of the arrays emulated the desired signal and the other emulated the interference, observing that the errors were more significant at higher signal-to-noise ratios. Additionally, the zero-forcing algorithm was more sensitive to errors than the matched filter, which was expected since the accuracy of the former for interference suppression is critical.

Index Terms—OTA, automotive, precoding, excitation errors.

I. INTRODUCTION

Over-The-Air (OTA) testing has become the standard method for full performance evaluation of wireless devices. It accounts for the antenna characteristics of the Device Under Test (DUT) in an environment that emulates its actual use. Besides testing the communication protocols and the performance of the radio frequency part, it may also consider other sources of error such as using its own power source [1].

OTA is a key enabler of the development of the automotive industry, especially as it is moving towards the integration of an increasing number of sensors, i.e., radars, lidars, cameras, as well as wireless communications and GPS. Radars will be mostly used in the 76 – 81 GHz range since the 24 GHz ultra-wideband has been phased out this January [2]. However, many other products still operate in the lower Millimeter Wave (mmWave) bands and below, including Vehicle-to-Everything (V2X) communications, which operate in the sub-6 GHz bands for now. Nevertheless, there is a need for larger data rates than those achieved by sub-6 GHz bands to support applications such as exchanging raw data from sensors in vehicles. This can be achieved by resorting to the mmWave frequencies, such as the already defined FR2 frequency bands [3].

Currently, there are OTA testing systems available for mmWave communications, e.g., [4] and [5]. There are already solutions for mmWave radar testing too [6], including car-mounted ones [7]. However, to the best of the authors' knowledge, and in agreement with [1], there are no available solutions for FR2 communications automotive OTA testing that are feasible in terms of hardware costs and dimensions, so further efforts must be made to devise such solutions.

In this paper we present numerical simulations of an OTA system at 28 GHz, corresponding to the center frequency of the 3GPP n257 band, chosen as a representative of FR2. One of the main challenges for automotive OTA, especially for vehicle-in-the-loop testing, is fulfilling the far-field criterion, i.e., the Fraunhofer distance. For a whole car at mmWave, it extends to several km. Clearly, these distances are not feasible in a controlled environment. Thus, there is a need to resort to OTA techniques that, while not physically being in the far-field, can emulate an impinging plane wave at the automobile. Among such techniques, there are compact test ranges, plane wave generators and random line-of-sight (usually denoted in the literature as RLOS, Random-LOS, or Ranlos). We take the approach of the Random-LOS technique [8], [9], [10].

In this work, we first conduct a study of the combined effects of linear chamber array size and the distance between the center of the chamber array and the center of the Test Zone (TZ) for a given TZ size. The performance criteria is a set of Figures of Merit (FoM) that evaluate the similarity of the field emulated in the TZ to a plane wave. The idea is to find the most compact set, i.e., the smallest array and shortest distance (at least shorter than Fraunhofer distance) that satisfies the accuracy criteria. We also study the tolerance in terms of FoM compliance of a subset of distances and chamber array sizes to random complex excitation errors of the chamber array due to, e.g., manufacturing tolerances and quantization errors. We also study the impact of errors on the performance of Matched Filter (MF) and Zero Forcing (ZF) algorithms due to complex errors in the weights of the DUT array. The results show that chamber array excitation errors must be considered when selecting distances and chamber array sizes, and also that DUT errors affect significantly more to ZF than to MF.

II. OTA SETUP AND FOM FOR TZ QUALITY EVALUATION

A. OTA setup

The basic arrangement of the OTA setup is depicted in Fig. 1, which is not to scale. The chamber array is defined as a uniform linear array along the x -axis, with a fixed number

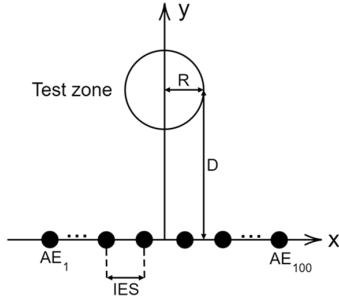


Fig. 1. Initial OTA setup

of Antenna Elements (AEs) $N_C = 100$. The AEs are idealized vertically polarized isotropic radiators operating at 28 GHz. A linear taper from 0 dB to -6 dB is applied to 25 elements on each side of the array to reduce field fluctuations in the TZ as explained in Section II-C [11]. Thus, the Electric Field (EF) at a given point P , accounting only for the vertical polarization (z -axis), is computed by the superposition principle as

$$E_z = \sum_{i=1}^{N_C} t_{c_i} E_0 \frac{e^{-jkr_i}}{4\pi r_i} = \sum_{i=1}^{N_C} t_{c_i} \frac{e^{-jkr_i}}{4\pi r_i}, \quad (1)$$

where E_0 is set to 1 for simplicity, $t_{c_i} = 10^{t_{c_i \text{ dB}}/20}$ is the tapering coefficient in linear scale of the i -th AE, being $t_{c_i \text{ dB}}$ the dB-scale tapering coefficient, and r_i is the distance between the i -th AE and P . Inter-Element Spacing (IES) is considered a variable, ranging from 0.5λ to 1.5λ , with 0.05λ step, resulting in a variable chamber array length $L = (N_C - 1)IES$. The TZ is contained by the XY -plane and it is defined as a circle of radius $R = (N_C - 1)IES/4$, where IES equals 0.5λ . Hence, $R = 99\lambda/8 = 13.26$ cm is a quarter of the length of the shortest considered chamber array. The center of the TZ is at a distance D of the chamber array, along the y -axis.

B. FoM for the TZ

The objective of this OTA setup is to emulate an EF distribution over the TZ that emulates a plane wave. To assess the accuracy of the plane wave, several FoM are defined. First, we consider

$$R_{mag} = \max(20 \log_{10} (|\mathbf{E}_z|)) - \min(20 \log_{10} (|\mathbf{E}_z|)), \quad (2)$$

where \mathbf{E}_z is the EF of every sample belonging to the TZ. R_{mag} defines the dynamic range of the magnitude of the EF samples in the TZ. These samples come from the nodes of a mesh with equal $\lambda/8$ interval in both the x - and y -axes, so the density of samples is constant over the circular TZ area.

Secondly, we evaluate the standard deviation of the magnitude of the EF samples in the TZ in dB

$$\sigma_{mag} = \sqrt{\frac{\sum_{s=1}^{N_s} (X_s - \bar{x})^2}{N - 1}}, \quad (3)$$

where N is the number of samples in the TZ, X_s is the EF magnitude in logarithmic units of the s -th sample, and \bar{x} is

the mean of the EF magnitude over all the TZ samples. This FoM is supported by the 3GPP [12].

Thirdly, we compute the dynamic range of the phase of the EF over the TZ

$$R_{phs_{rows_n}} = \max(\angle \mathbf{E}_{z_n}) - \min(\angle \mathbf{E}_{z_n}), \quad (4)$$

$$R_{phs} = \max(\mathbf{R}_{phs_{rows}}), \quad (5)$$

where \mathbf{R}_{phs} contains the phase range over each parallel stripe (with respect to the chamber array) of samples of the TZ, $R_{phs_{rows_n}}$ is the phase range of a given parallel stripe, \mathbf{E}_{z_n} contains the EF values of a given parallel stripe, and \angle denotes the phase value or angle. This FoM may arise a concern due to the periodic nature of the phase. Indeed, if wrapped up to the interval $[0^\circ, 360^\circ]$, then one could argue that, e.g. if within a row, there is a phase value of 359° and other value of 2° , the resulting $R_{phs_{rows_n}}$ would be 357° . This has been taken into account, so that the correct variation, of 3° in this case, is always computed. We limit the variation to 180° because that is the maximum phase deviation that can actually occur.

It is worth noting the ideal values of the FoM. Since the desired EF distribution is that of a plane wave, the magnitude of the EF over the TZ should be the same, so R_{mag} and σ_{mag} should be 0 dB. Similarly, the phase should be constant along each parallel stripe, so $R_{phs} = 0^\circ$. However, a perfect plane wave EF distribution is not achievable due to physical limitations, e.g., finite aperture and a number of sources. Thus, we focus on acceptable FoM values: $R_{mag} \leq 1$ dB is commonly accepted [13], while $\sigma_{mag} \leq 0.25$ dB is, according to [12], required, and $R_{phs} \leq 10^\circ$ is often assumed as an acceptable limit [14].

C. L and D satisfying the FoM limits

Having defined the FoM and their acceptable values, we investigate the L and D combinations that fulfill them for the considered OTA setup. This study is extended to stricter acceptable values, paving the way for the study described in Section III, where the use of these stricter values is justified. The study consists in varying the IES between 0.5λ and 1.5λ , with 0.05λ step, resulting in the variation of L , varying D from 40 to 2450λ . The maximum D value corresponds to roughly half the shortest Fraunhofer distance, i.e. the one for the shortest considered chamber array, which has an IES of 0.5λ . The FoM values are computed for each L and D combination and evaluated against the FoM acceptable values.

The goal is to find an OTA test setup which is as compact as possible in terms of antenna size L and chamber dimensions, roughly defined by D . The considered values of D are significantly lower than the shortest Fraunhofer distance. It is worthwhile to note that no optimization has been carried out, so the chosen combinations of L and D can be further improved, e.g., by the use of more advanced tapering techniques and by applying actual computational optimization techniques like the ones used in [15], [16].

As shown in [11], linear tapering is an effective technique to reduce EF variations. Indeed, the L and D values fulfilling the

III. STUDY OF CHAMBER ARRAY EXCITATION ERRORS

A. Error model

A study of excitation errors of the chamber array can be found, e.g., in [14], [17]. The study conducted in this paper aims at quantifying the chamber array excitation error that can be tolerated by the selected L and D combinations. The error model in this paper is different from the ones presented in the references above, thus the results are not directly compared. In [14] two normally distributed random variables with the same standard deviation were used, which is good for simplicity. Nevertheless, the error is made proportional to the weighting coefficient, which adds complexity to the analysis. In [17], separated amplitude and phase error normally distributed random variables are assumed, each with its own standard deviation, which is impractical for the study conducted in this paper, since this would make this study two-dimensional, unnecessarily increasing the complexity.

For the sake of simplicity, the error model in this paper comprises a normally distributed complex random variable given by

$$\epsilon_{ch_i} = \mathcal{N}(0, \sigma_{ch}) + j\mathcal{N}(0, \sigma_{ch}), \quad (6)$$

where ϵ_{ch_i} is the excitation error of the i -th element of the chamber array, so a different realization of the excitation error is used for each of the AEs of the chamber array, and σ_{ch} is the standard deviation of the excitation error. For similarity with [14], the standard deviation will be increased in dB-scale $\sigma_{ch_{dB}}$. Hence,

$$\sigma_{ch} = 10^{\sigma_{ch_{dB}}/20} - 1. \quad (7)$$

Therefore, the EF expression at a given point P , is now computed as

$$E_z = \sum_{i=1}^{N_C} (1 + \epsilon_{ch_i}) t_{c_i} \frac{e^{-jkr_i}}{4\pi r_i}. \quad (8)$$

B. Simulation results

Monte-Carlo simulations were conducted for each selected combination of L and D shown in Fig. 2 (b) and (c), where $\sigma_{ch_{dB}}$ was progressively increased with 0.01 dB step. The FoM were computed at each step and compared against the limits, i.e., $\sigma_{mag} \leq 0.25$ dB, $R_{mag} \leq 1$ dB, and $R_{phs} \leq 10^\circ$. When any of the FoM does not comply with these values, then the value of $\sigma_{ch_{dB}}$ of the previous iteration is stored. The reason of not using the L and D from Fig. 2 (a), is that some

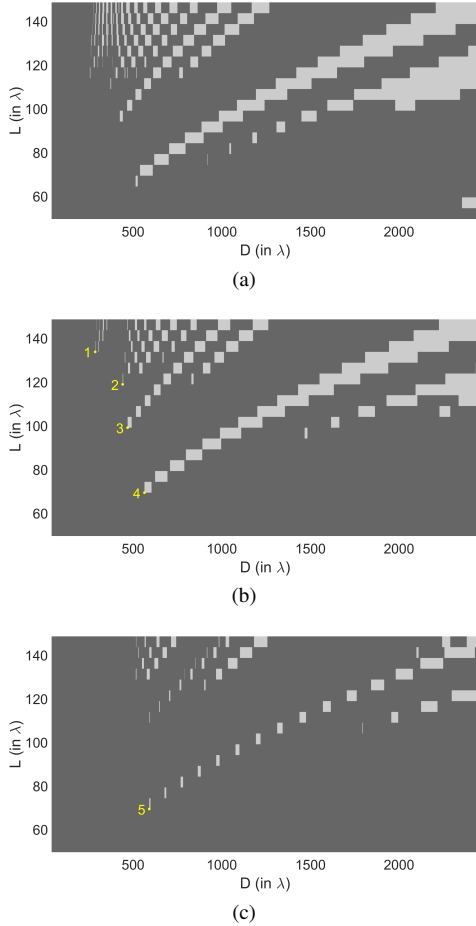


Fig. 2. L and D values compliant with all FoM limits in light grey. (a) $\sigma_{mag} = 0.25$ dB, $R_{mag} = 1$ dB, $R_{phs} = 10^\circ$, (b) $\sigma_{mag} = 0.225$ dB, $R_{mag} = 0.9$ dB, $R_{phs} = 9^\circ$, (c) $\sigma_{mag} = 0.2$ dB, $R_{mag} = 0.8$ dB, $R_{phs} = 8^\circ$. Note that in (b) and (c), the points used for Sections III and IV are marked.

FoM limits were significantly lower than without tapering. The results from this study are shown in Fig. 2. Note that each point marked in yellow corresponds to one of the 5 chosen L and D combinations for Sections III and IV. From these results, it can be observed that, due to the highly non-linear nature of the aggregation of the EF generated by these 100 sources, while still being in the near-field, there are discontinuities in the L and D combinations. I.e., for a given value of L , intuitively one would think that if a value of D fulfills the FoM limits, then a larger value of D should fulfill them too, but that is not generally the case. On the other hand, there is some continuity in the ratios of L and D that fulfill the FoM limits, forming a series of somewhat continuous “curves” that fulfill the FoM. Finally, if we focus only on the most compact possible setups, i.e., lowest L and D combinations, marked in yellow, it can be observed that there is a trade-off between L and D , so a smaller chamber array requires a larger distance, and vice versa.

TABLE I
RESULTS OF MONTE-CARLO SIMULATIONS OF TOLERABLE $\sigma_{ch_{dB}}$ FOR L AND D COMBINATIONS FROM FIG. 2 (B) AND FIG. 2 (C)

L	IES	D	$\sigma_{ch_{dB}}$	FoM failed
1.43 m / 133.65 λ	1.35 λ	3.06 m / 286 λ	0.05 dB	R_{mag}
1.27 m / 118.8 λ	1.2 λ	4.73 m / 441 λ	0.12 dB	R_{mag}
1.06 m / 99 λ	λ	5.03 m / 469 λ	0.11 dB	R_{mag}
0.74 m / 69.3 λ	0.7 λ	6.04 m / 564 λ	0.24 dB	R_{phs}
0.74 m / 69.3 λ	0.7 λ	6.33 m / 591 λ	0.5 dB	R_{phs}

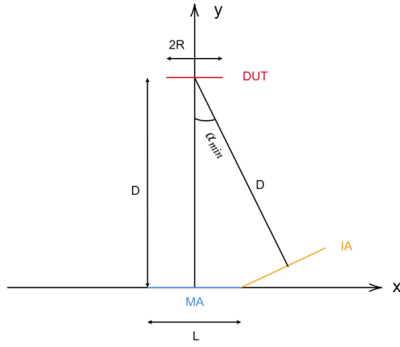


Fig. 3. MF and ZF performance study setup

of the best L and D combinations in terms of the compactness of the setup, did not even tolerate a $\sigma_{ch_{dB}}$ value of 0.01 dB, so more restrictive values of FoM were used in Fig. 2 (b) and (c) to ensure some headroom for excitation errors. The results of this study are shown in Table I, where each of the five points marked in Fig. 2 (b) and (c) corresponds, in order, with each of its rows. It can be observed that not all the L and D combinations from Fig. 2 (b) tolerate the same amount of standard deviation of the excitation error, even though all of them, in absence of excitation error, fulfill the same level of FoM. Additionally, the fifth L and D combination is, as one could intuitively think, the one with more resilience to this error, due to its larger headroom in FoM levels.

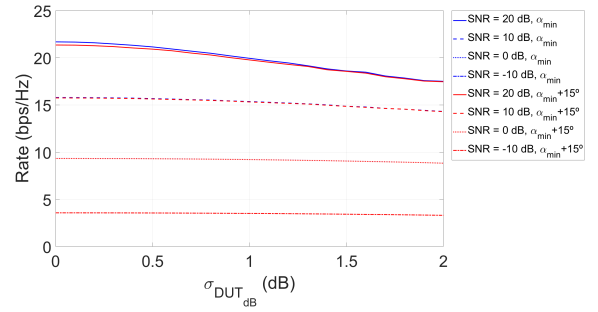
IV. STUDY OF DUT WEIGHT ERRORS

A. Setup

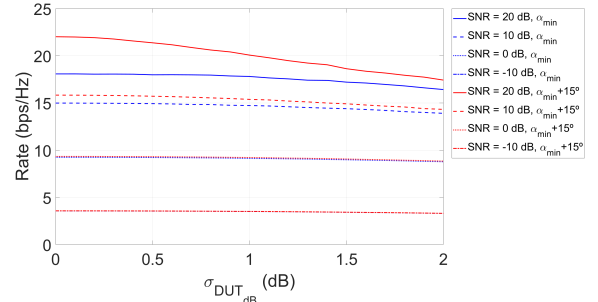
In this study, we consider a setup similar to the one shown in Fig. 1. Here, a second chamber array was used to emulate an interferer, and thus it is denoted as Interferer Array (IA). By design, it is identical to the Main Array (MA) and is placed at its side, as can be seen from Fig. 3. The chosen L and D define the minimum angle α_{min} . A generic DUT array antenna is placed in the TZ, and parallel to the main chamber array. The DUT consists of 49 vertically polarized idealized isotropic AEs. The considered L and D combinations are the ones from Section II and are shown in Fig. 2 and Table I. Additional placements of the IA are considered by increasing α_{min} by 15° for each L and D combinations.

B. Method

In this section, we aim at analyzing the impact of weight errors at the DUT on the performance of evaluated precoding algorithms. For this purpose, we assume that the MA and the IA emulate two user equipment, while the DUT is going to play the role of a base station. It could also represent two access points communicating with the onboard (on a vehicle) communications unit. Furthermore, in order to assess the impact of weight errors, we are going to measure the uplink sum rate. In order to do this, the channel matrix \mathbf{H} is first computed according to (1), obtaining the E_z values at each

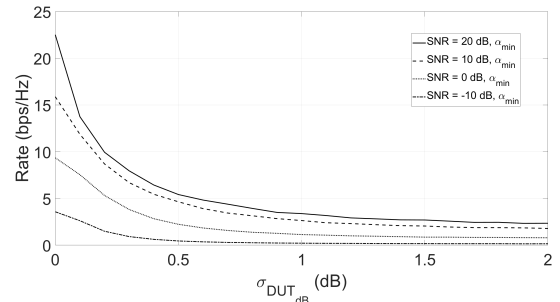


(a)



(b)

Fig. 4. MF average sum rate as a function of $\sigma_{DUT_{dB}}$, for different SNR levels and for both positions of the IA (α_{min} and $\alpha_{min} + 15^\circ$). (a) L and D from first row of Table I: $L = 133.65\lambda$, $D = 286\lambda$. (b) L and D from fifth row of Table I: $L = 69.3\lambda$, $D = 591\lambda$.



(a)

Fig. 5. ZF average sum rate as a function of $\sigma_{DUT_{dB}}$, for different SNR levels. L and D from first row of Table I: $L = 133.65\lambda$, $D = 286\lambda$.

AE of the DUT, from the MA and the IA. After that, the weights are computed for both MF and ZF, according to:

$$\mathbf{W}_{MF} = \mathbf{H}^\dagger, \quad (9)$$

$$\mathbf{W}_{ZF} = \mathbf{H}^\dagger (\mathbf{H}\mathbf{H}^\dagger)^{-1}. \quad (10)$$

After this, \mathbf{W} is distorted by an error statistically distributed as the one already presented in Section III-A. However, now the standard deviation is named as $\sigma_{DUT_{dB}}$, and varied from 0 – 2 dB, with 0.1 dB step. The other variable is the SNR, which is evaluated at -10 , 0 , 10 and 20 dBs. The Signal to Interference plus Noise Ratio (SINR) for the MA and the IA is computed for each combination of $\sigma_{DUT_{dB}}$ and SNR and,

after that, the sum rate is computed according to

$$SR = \sum_{u=1}^2 \log_2(1 + SINR_u), \quad (11)$$

where the subscript u refers to the chamber arrays (MA and IA). The same procedure was repeated for all the iterations of the Monte-Carlo simulations, with the corresponding averaging of the sum rate afterward. This is repeated for all the L and D combinations, as well as the different IA placements.

C. Results

As expected, the performance of MF and ZF is impacted by the weighting errors of the DUT array. However, it depends on the SNR, and, as can be seen from Fig. 4 and Fig. 5, this impact is much higher for ZF than for MF. The results for all L and D combinations show some differences in some cases and only for MF, finding no relevant changes for ZF. As for the two considered angles α_{min} and $\alpha_{min} + 15^\circ$, they follow the same trend as the L and D combinations, having only relevant differences for some of the L and D combinations and only for MF. Therefore, to illustrate the most relevant case in terms of difference of results, the results for L and D combinations corresponding to the first and fifth rows of Table I for MF are shown in Fig. 4 (a) and Fig. 4 (b), respectively, with the two considered angles. For ZF, due to the similarity of all results, i.e. for all L and D combinations and both considered angles, only the L and D combination belonging to the first row of Table I and only for the α_{min} angle is presented in Fig. 5.

In Fig. 4, it can be seen that the impact of the MF weighting errors on the sum rate is only relevant for large SNRs. Additionally, the L and D combination of Fig. 4 (a) shows that the performance of MF is very similar for both positions of the IA. On the other hand, for the L and D combination of Fig. 4 (b), the performance of MF suffers more.

In Fig. 5, the impact of ZF weighting errors on sum rate is relevant for all SNRs, with similar behaviour, although affecting more to higher SNRs. In any case, the weighting error impact is larger for ZF than for MF across the board.

V. CONCLUSION

In this paper, we have shown that the errors due to the chamber array excitation weights may affect the feasible size of the chamber array and the distance between the test zone center to the chamber array center, i.e., the size of the testing facility. It was concluded that not all feasible combinations of these two parameters will be resilient to the chamber array errors to the same degree. It was also shown the impact on the performance of weighting coefficients errors of the DUT array in terms of sum rate for matched filter and zero-forcing precoding algorithms, concluding that zero-forcing is, in general, much more sensitive than a matched filter to such errors. It was also concluded that the impact of weighting errors increased with the signal-to-noise ratio. We hope that the current paper paves the further steps toward future over-the-air testing solutions, especially for automotive applications. Testing solutions using FR2 frequencies for communications

will benefit from the presented findings when focusing on having an over-the-air testing solution that is as compact as possible while considering different sources of error in the design process.

ACKNOWLEDGMENT

The work of Alejandro Antón was conducted within the ITN-5VC project, which is supported by the European Union's Horizon 2020 research and innovation program under the Marie Skłodowska-Curie grant agreement No. 955629.

REFERENCES

- [1] P. Pelland, D. J. van Rensburg, M. Berbeci, F. O. Storjohann, A. Grieseche, and J.-P. Busch, "Automotive OTA Measurement Techniques and Challenges," in *2020 Antenna Measurement Techniques Association Symposium (AMTA)*, 2020, pp. 1–6.
- [2] ETSI EN 302 288, "Short Range Devices; Transport and Traffic Telematics (TTT); Ultra-wideband radar equipment operating in the 24,25 GHz to 26,65 GHz range; Harmonised Standard covering the essential requirements of article 3.2 of Directive 2014/53/EU." 2017.
- [3] J. Choi, V. Va, N. Gonzalez-Prelcic, R. Daniels, C. R. Bhat, and R. W. Heath, "Millimeter-Wave Vehicular Communication to Support Massive Automotive Sensing," *IEEE Communications Magazine*, vol. 54, no. 12, pp. 160–167, 2016.
- [4] Bluetest. (2023) BLUETEST RTS65. The ultimate OTA system. [Online]. Available: <https://www.bluetest.se/products/chambers/rts65/>
- [5] Rohde&Schwarz. (2022) R&S@ATS1800C Compact 3GPP-compliant OTA chamber for 5G NR mmWave signals. [Online]. Available: https://www.rohde-schwarz.com/products/test-and-measurement/antenna-test-systems-and-ota-chambers/rs-ats1800c-compact-3gpp-compliant-ota-chamber-for-5g-nr-mmwave-signals_63493-687744.html
- [6] Rohde&Schwarz. (2022) R&S@ATS1500C Antenna test chamber for automotive radar. [Online]. Available: https://www.rohde-schwarz.com/products/test-and-measurement/antenna-test-systems-and-ota-chambers/rs-ats1500c-antenna-test-chamber-for-automotive-radar_63493-713188.html
- [7] S. B. J. Gowdu, M. E. Asghar, R. Stephan, M. A. Hein, J. Nagel, and F. Baumgärtner, "System architecture for installed-performance testing of automotive radars over-the-air," in *2018 IEEE MTT-S International Conference on Microwaves for Intelligent Mobility (ICMIM)*, 2018, pp. 1–4.
- [8] M. S. Kildal, S. M. Moghaddam, J. Carlsson, J. Yang, and A. A. Glazunov, "Evaluation of a random line-of-sight over-the-air measurement setup at 28 ghz," *IEEE Transactions on Antennas and Propagation*, vol. 69, no. 8, pp. 5008–5020, 2021.
- [9] M. S. Kildal, J. Carlsson, and A. Alayón Glazunov, "Measurements and Simulations for Validation of the Random-LOS Measurement Accuracy for Vehicular OTA Applications," *IEEE Transactions on Antennas and Propagation*, vol. 66, no. 11, pp. 6291–6299, 2018.
- [10] M. S. Kildal, S. Mansouri Moghaddam, A. Razavi, J. Carlsson, J. Yang, and A. Alayón Glazunov, "Verification of the Random Line-of-Sight Measurement Setup at 1.5-3 GHz Including MIMO Throughput Measurements of a Complete Vehicle," *IEEE Transactions on Vehicular Technology*, vol. 69, no. 11, pp. 13 165–13 179, 2020.
- [11] A. A. Glazunov, P.-S. Kildal, and M. S. Kildal, "Devising a horizontal chamber array for automotive ota tests in random line-of-sight," in *2015 International Symposium on Antennas and Propagation (ISAP)*, 2015, pp. 1–4.
- [12] 3GPP. Technical report TR 37.941 V16.2.0, "Radio Frequency (RF) conformance testing background for radiated Base Station (BS) requirements." 2020.
- [13] O. M. Bucci, M. D. Migliore, G. Panariello, and D. Pinchera, "Plane-Wave Generators: Design Guidelines, Achievable Performances and Effective Synthesis," *IEEE Transactions on Antennas and Propagation*, vol. 61, no. 4, pp. 2005–2018, 2013.

- [14] O. A. Iupikov, P. S. Krasov, A. Alayón Glazunov, R. Maaskant, J. Friden, and M. V. Ivashina, "Hybrid OTA Chamber for Multi-Directional Testing of Wireless Devices: Plane Wave Spectrum Generator Design and Experimental Demonstration," *IEEE Transactions on Antennas and Propagation*, pp. 1–1, 2022.
- [15] M. Poordaraee and A. A. Glazunov, "Chamber array antenna layout for compact ota measurements," in *2020 14th European Conference on Antennas and Propagation (EuCAP)*, 2020, pp. 1–4.
- [16] M. Poordaraee and A. A. Glazunov, "Plane wave synthesis with irregular chamber planar antenna arrays for compact ota measurements," in *2019 13th European Conference on Antennas and Propagation (EuCAP)*, 2019, pp. 1–5.
- [17] G. He, X. Gao, and R. Zhang, "Impact Analysis and Calibration Methods of Excitation Errors for Phased Array Antennas," *IEEE Access*, vol. 9, pp. 59 010–59 026, 2021.